A Coupled Thermal and Mechanical Model of Sliding Wear

S. S. Akarca, W. J. Altenhof, and A. T. Alpas
Department of Mechanical, Automotive, & Materials Engineering,
University of Windsor, 401 Sunset Avenue, Essex Hall, Windsor ON, Canada N9B 3P4

Abstract

Sliding wear of aluminum alloys induce plastic deformation below the contact surfaces even at light loads. Experimental evidence exists for damage accumulation in the form of nucleation of voids and microcracks around the second phase particles in the material layers adjacent to the contact surface. Crack propagation at a certain depth below the surface may lead to the creation of long and thin wear debris particles. The objective of this work was to study deformation and damage accumulation processes in aluminum alloys during sliding wear. LS-DYNA was used to model multiple sliding contacts between an aluminum alloy and a steel counterface. The material model used in the finite element analysis was based on the stress/strain behaviour of a 356 Al (Al-7%Si) alloy determined directly from the analysis of the deformation state of the subsurfaces generated during sliding wear tests. Strain rate and thermal effects were also considered through a coupled thermal and mechanical analysis using material type 106 in LS-DYNA (*MAT_ELASTIC_ VISCOPLASTIC_THERMAL). The accumulation of stresses and strains were studied as a function of contact cycle number.

The Lagrangian thermal and mechanical coupled finite element model developed in LS-DYNA was successful to simulate deformation of the aluminum alloy during sliding contacts. Subsurface distributions of the hydrostatic pressure, strain rate and temperature, which are difficult to characterize experimentally or theoretically for work hardening materials, were determined for different loading conditions during sliding contacts. Predicted distributions of stresses and strains were used to model subsurface damage gradient and delamination of subsurface layers. Numerical investigation of a void growth model based on a ductile void growth theory showed the presence of a damage gradient and a critical depth at which delamination cracks might initiate and propagate.

Introduction

Aluminum-silicon alloys are used in many vehicle parts including engine blocks, cylinder liners, connecting rods, pistons, gears and valves, primarily due to their high strength to weight ratio and good castability. Some of these components are subjected to sliding motion. Relatively low wear resistance of the aluminum-silicon alloys compared to steels is a factor that was restricted more widespread applications of these alloys in parts operating in sliding contact conditions. Sliding wear is a complex form of wear which incorporates several physical, chemical and thermal events. Plate-like thin flake debris formation is commonly observed in a sliding wear system (Figure 1). Researches has shown that, under dry or poorly lubricated sliding conditions, cracks initiating from secondary particles or inclusions propagate parallel to the surface to form wear particles of thin flake shape [1-8]. In order to quantify this debris formation processes, distributions of the subsurface stresses and strains need to be determined. Experimental determination of the subsurface deformation state is very challenging. Analytical and theoretical solutions to the contact stress fields have limited applications in this area due to the assumptions made to reach a solution. Numerical methods like the finite element method are promising approaches to solve the short comings of theoretical solutions.

The present study was carried out to investigate subsurface deformation and damage accumulation events observed in the dry sliding wear of aluminum alloys. LS-DYNA was used to model multiple sliding contacts between an Al-Si half-space (a 356 Al type alloy) and a steel counterface. The material model used in the finite element analysis was based on the stress/strain

behaviour of a 356 Al (Al-7%Si) alloy determined directly from the analysis of the deformation state of the subsurfaces generated during sliding wear tests. Strain rate and thermal effects were also considered through a coupled thermal and mechanical analysis.

Finite Element Model Geometry

The finite element model used in the coupled thermo-mechanical analysis of the sliding contact consisted of two main parts, the Al-Si half-space and the steel counterfaces. The sliding contact was modeled by pressing a rigid steel surface in semi-cylindrical shape of 2.0 mm diameter on a 356 Al surface of 2.9 x 13.3 mm^2 and then sliding the counterface over the half-space surface repeatedly at a constant sliding velocity. The third dimension of the model was assumed infinite (plane strain condition). A schematic view of the set-up is shown in Figure 2.

Element Formulation and Properties

The numerical model used 2D solid elements. Lagrangian solid element formulation type 13 (plane strain element formulation) (ELFORM:13) in LS-DYNA [9] was used with four Gaussian integration points. Options for the thermal solution were set in *CONTROL_ THERMAL_SOLVER card where a transient thermal analysis type was defined. Eight Gaussian points per element were specified for the thermal analysis calculations.

Material Model

Strain rate and thermal effects were taken into account in the numerical material model using material type 106 in LS-DYNA (*MAT_ELASTIC_VISCOPLASTIC_ THERMAL) [9]. A constitutive equation, which consists of the experimentally defined Voce type stress-strain relationship [8] combined with Cowper and Symond type [10] strain rate equation and Johnson-Cook type [11] temperature relation, was used:
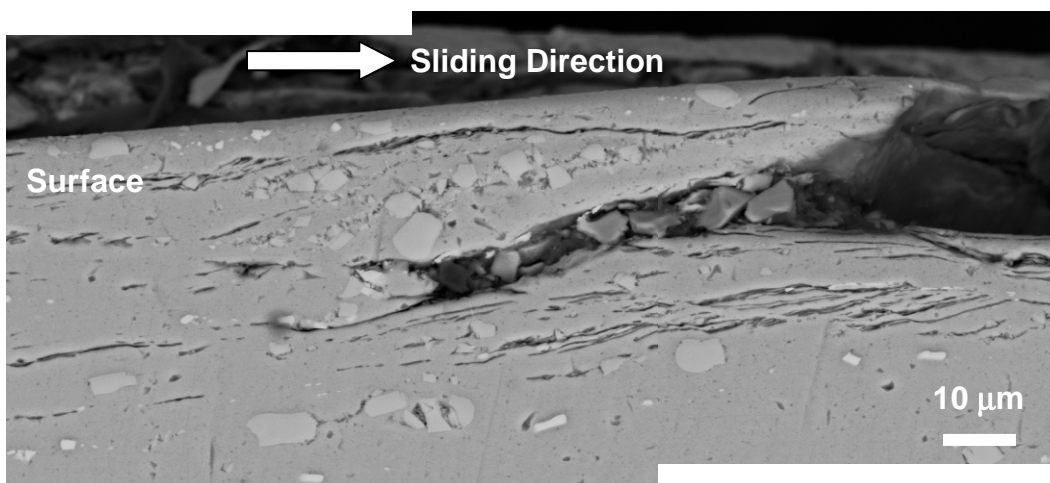

Figure 1: Subsurface crack propagation observed in a 356 Al alloy during dry sliding wear.

$$\sigma_f = \left[\sigma_S - (\sigma_S - \sigma_0) \exp\left(-\frac{\varepsilon}{\varepsilon_C} \right) \right] \left[1 + \left(\frac{\dot{\varepsilon}^p}{D} \right)^{1/q} \right] \left[1 - \left(\frac{T - T_{room}}{T_{melt} - T_{room}} \right)^m \right] \tag{1}$$

In Equation 1, the expression in the first set of brackets represents the strain hardening behaviour under the athermal conditions where σ_f is the flow stress (effective stress), ε is the equivalent plastic strain, σ_0 (= 240 MPa) is the bulk flow strength, and σ_S (= 400 MPa) is the saturation stress (the stress at which the work hardening rate becomes zero). ε_C is a material constant and was observed to be equal to 4.79 for the 356 Al material [8]. The expressions in the second and third sets of brackets represent the strain rate hardening and the thermal softening effects on the flow stress where $\dot{\varepsilon}^p$ is the plastic strain rate in s^{-1} units, D (s^{-1}) and q are the Cowper and Symond material parameters. T (K) is the temperature of the contacting material, T_{room} is the room temperature, T_{melt} is the melting temperature (K) and m is the dimensionless Johnson-Cook thermal material parameter. Material parameters for strain rate hardening in Equation 1 taken from the literature were D = 6500 s^{-1} and q = 4 for the 356 Al alloy [12]. The temperature coefficients were taken from the work of Johnson and Cook [11] where the thermal material parameter (m) was determined as 1 for different aluminum alloys. The initial room temperature and the melting temperature of the 356 Al was 300 K and 828 K, respectively.

Figure 3 shows stress-strain-temperature relationships defined into the material model at constant strain rates of 0-10^5 s^{-1}. A zero strain rate implies that during sliding the material layers below the worn surfaces were not subjected to a strain rate in excess to the experimentally applied strain rate. Young's modulus (E), Poisson's ratio (ν) and mass density (ρ) of the 356 Al half-space were specified as 72.4 GPa, 0.33 and 2.669 Mg/m^3 respectively [8, 13]. The steel counterfaces were modeled as rigid materials (*MAT_RIGID) and the properties of the counterfaces were as follows E = 207 GPa, ν = 0.3 and ρ = 7.8 Mg/m^3. Ninety-five percent of the mechanical work was assumed to be converted into heat. Thermal material properties of the 356 Al alloy were determined from the literature and defined in an isotropic thermal material model (*MAT_THERMAL_ISOTROPIC) as follows; heat capacity: 963 J/kg·K, thermal conductivity: 151 W/m·K and coefficient of thermal expansion: 23.5 µm/m·K [13].

Loading and Boundary Conditions

The steel semi-cylindrical counterface was pressed on the aluminum half-space by applying a constant normal load of 150 N per mm thickness in the Y direction (Figure 2). The applied normal load was distributed equally on each node located at the top layer of the counterface (Figure 2). All nodes at the bottom of the 356 Al half-space were constrained in all degrees of freedom (Figure 2). A sliding velocity of 10m/s in the X direction was assigned to the steel counterface. Loading was prescribed in such a way that during each contact cycle the counterface was first loaded with a constant normal load and then translated with a constant sliding velocity over the half-space surface.

Adiabatic thermal boundary conditions were applied to the half-space. Both thermal and structural calculations were completed by doing a transient time dependent analysis [9]. The explicit time integration approach was used for the structural analysis and a fully implicit time integration scheme was utilized for the thermal analysis calculations [9]. For every ten explicit structural time steps completed, a thermal implicit time step calculation was performed.

Contact Algorithm

The contact between the steel and the aluminum entities was modeled using a two dimensional automatic type contact algorithm (*CONTACT_2D_AUTOMATIC_NODE_TO_SURFACE_ THERMAL) with the thermal option [9]. The 356 Al half-space was designated as the slave entity while the steel counterfaces were defined as the master entities for the numerical contact. Due to excessive nodal penetrations observed in initial trial simulations, the default value of the penalty scale factor was increased from 1.0 to 5.0 for the numerical models. In order to achieve a stable simulation, time step was lowered by changing time step scale factor from the default value of 0.9 to 0.8 in the *CONTROL_TIMESTEP card.

Results and Discussion

The variation of the subsurface von Mises stress with the depth of material below the contact surface after each contact cycle for a sliding velocity of 10 m/s and normal load of 150 N/mm are shown in Figure 4 where the steel counterface is at the mid point of the 356 Al half-space. The X-axis in Figure 4 is a dimensionless normalized depth (z/a), where z is the depth beneath the contact surface and a is the counterface diameter (= 2 mm). The von Mises stress at the contact surface was 513.6 MPa after the first contact, 585.5 MPa after the fourth and 596.9 MPa after the seventh. Subsurface von Mises stresses reached a steady state after the fourth contact: a 14 % increase occurred between the first and the fourth contacts, but only a 2 % increase occurred after the fourth. The maximum von Mises stress was positioned just under the counterface close to the leading edge.

Figure 5 shows the variation of plastic strains as a function of z/a at different contact cycles. The maximum value of plastic strain was found to be at the surface: 0.19, 0.78 and 1.30 for the first, fourth and seventh contacts. The plastic strains were less than 0.01 in the subsurface material layers at z/a > 0.2.

Hydrostatic pressure distribution at the mid point of the 356 Al alloy is shown in Figure 6 at different contact cycles. The value of the hydrostatic pressure at the contact surface did not change with increasing sliding contact numbers. It was 1150 ± 100 MPa between the first and the seventh contacts. The value of the hydrostatic pressure reduced very quickly with increasing z/a. At z/a > 0.1, it was less than the values of the von Mises stress.

The subsurface temperature distribution with contact cycles at mid point of the 356 Al half-space is presented in Figure 7. There was a total increase of 45 K at the surface after seven sliding contacts. The temperature dropped to 300 K at z/a = 0.135, 0.425, and 0.595 after the first, the fourth and the seventh contacts respectively. The surface temperature reached a steady state after the 5th sliding contact and there was only a 0.3 % increase in the temperature afterwards.
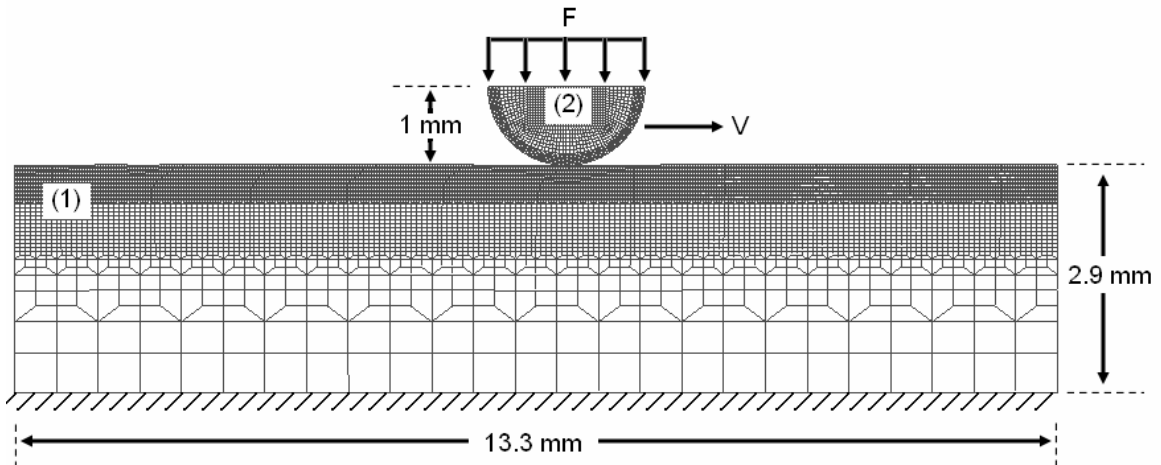
Figure 2: Geometry of the finite element model ((1) is the 356 Al half-space and (2) is the steel counterface), loading (F: Distributed normal load, V: Sliding velocity) and boundary conditions (restriction of the bottom nodes from the motion).
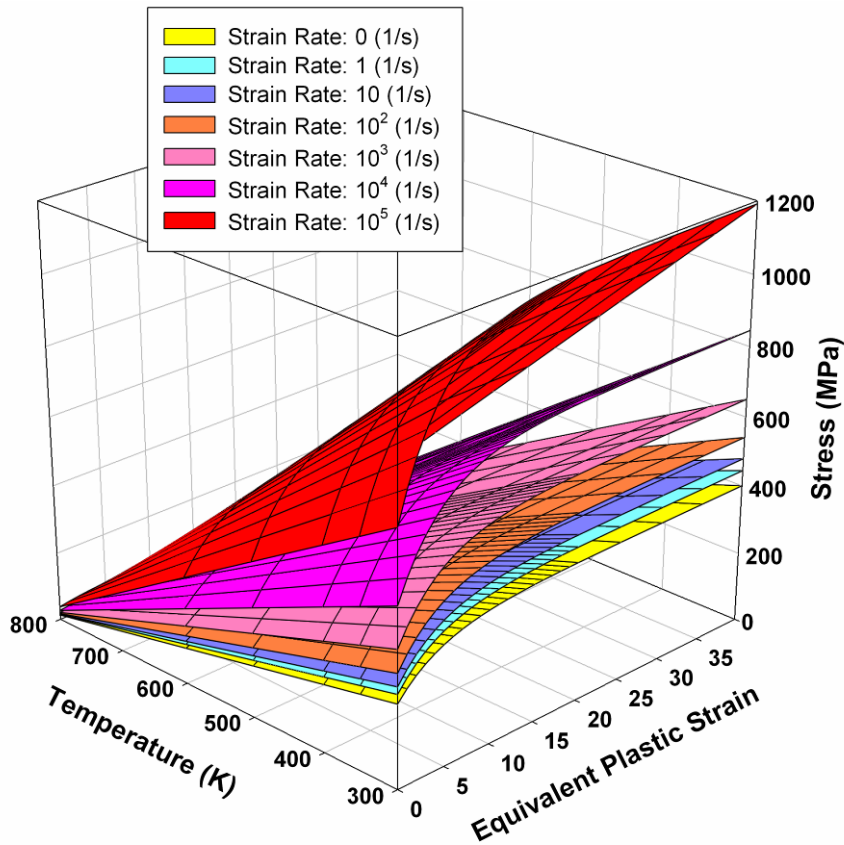

Figure 3: The relationships between the deformation parameters and temperatures obtained using Equation 1.
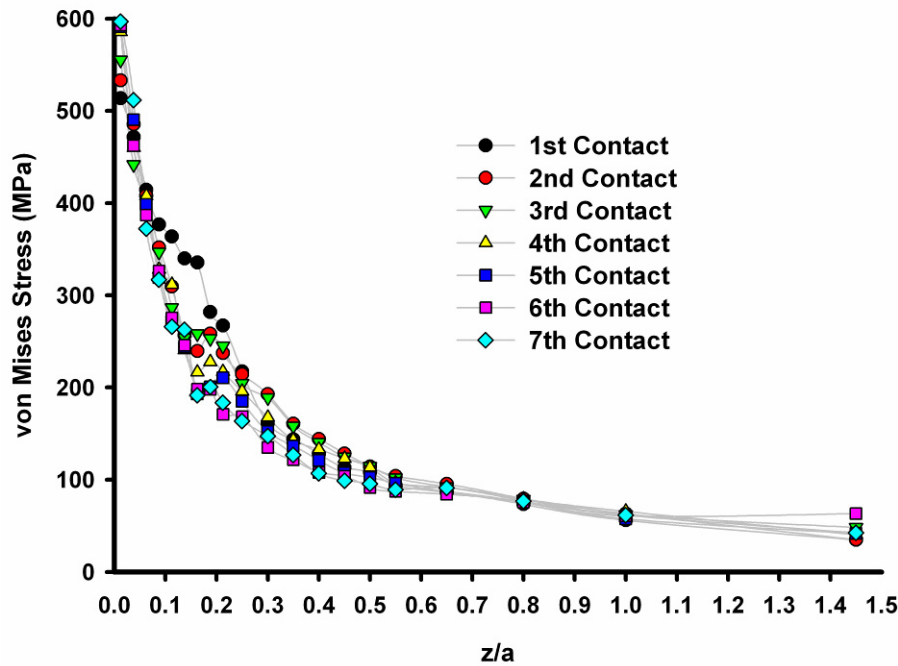
Figure 4: Accumulation of the subsurface stresses with increasing number of sliding contacts at the mid point of the 356 Al half-space (Sliding velocity: 10 m/s, Normal load: 150 N/mm). (z is the depth beneath the contact surface and a is the counterface diameter).
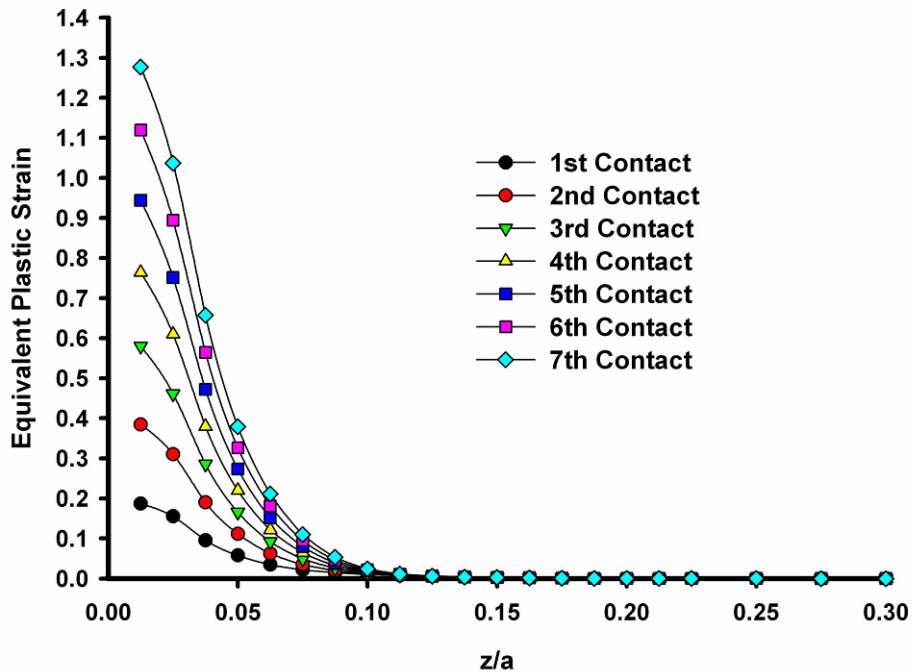

Figure 5: Accumulation of the subsurface equivalent plastic strains with increasing number of the sliding contacts at the mid point of the 356 Al half-space (Sliding velocity: 10 m/s, Normal load: 150 N/mm).
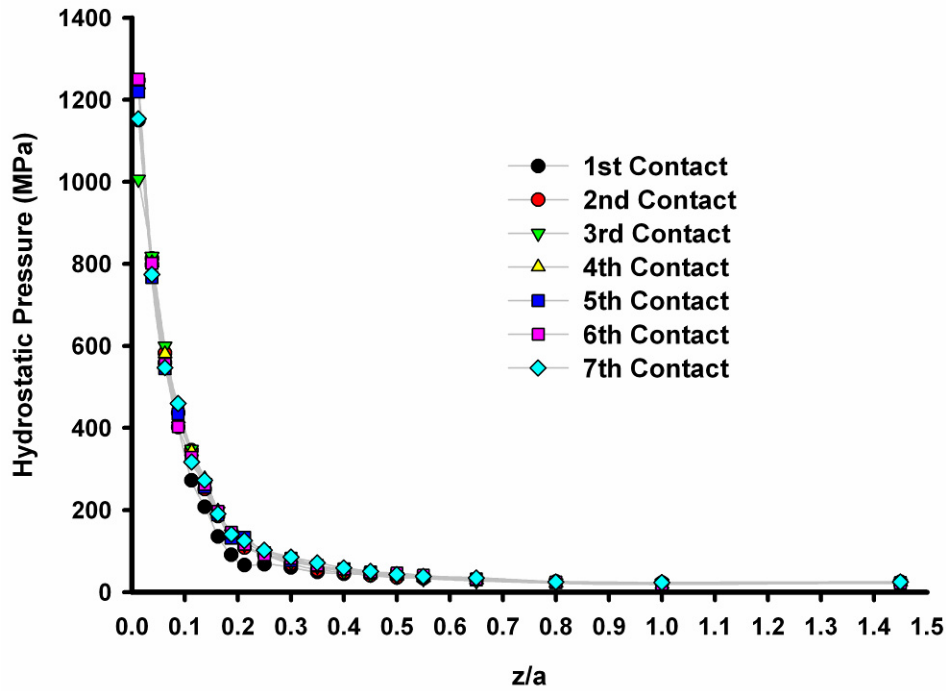
Figure 6: Distribution of the hydrostatic pressure with increasing number of sliding contacts at the mid point of the 356 Al half-space (Sliding velocity: 10 m/s, Normal load: 150 N/mm).
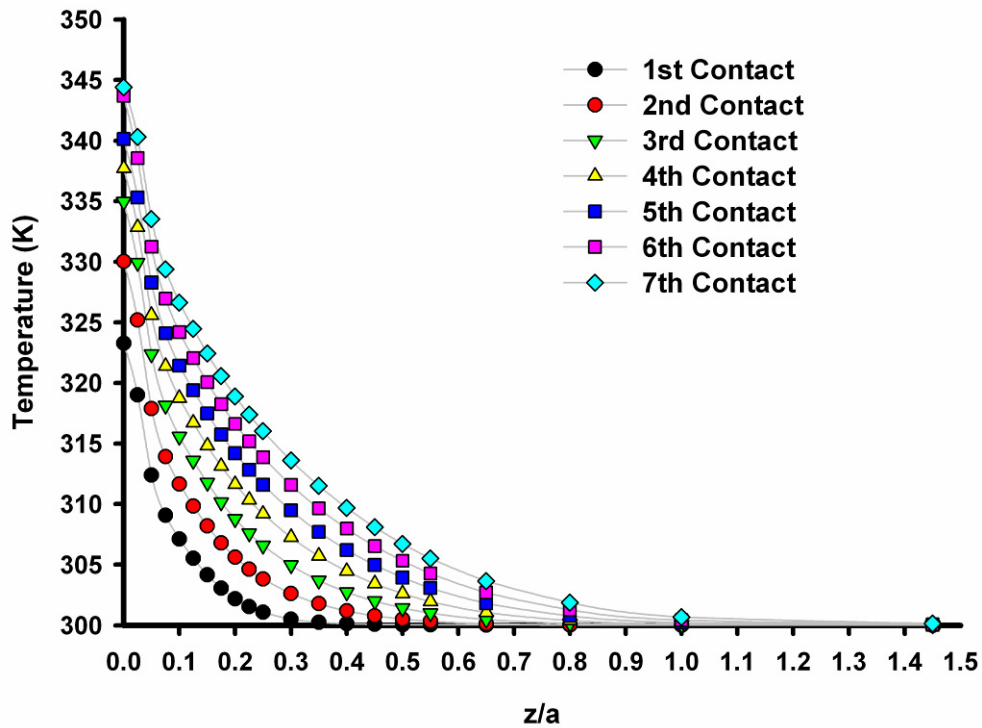

Figure 7: Increase of the subsurface temperature with multiple sliding contacts at the mid point of the 356 Al half-space (Sliding velocity: 10 m/s, Normal load: 150 N/mm).

Subsurface strain rates in the mid point of the 356 Al half-space are presented in Figure 8 for a sliding velocity 10 m/s and normal load of 150 N/mm. The strain rate ranged from 7.8 x 10^3 s^{-1} to 9.8 x 10^3 s^{-1} at z/a = 0.0125. The results indicated that the distribution of strain rate was independent of the sliding contact number after the second contact when the positions deeper than normalized depth of 0.05 (z/a>0.05) were examined.
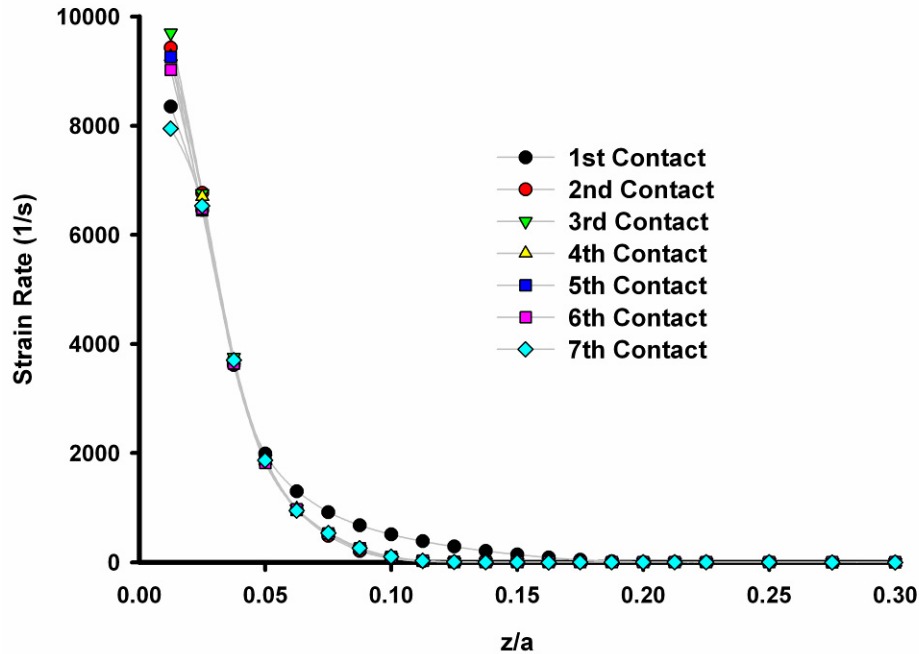

Figure 8: Change of the strain rate with multiple sliding contacts at the mid point of the 356 Al half-space (Sliding velocity: 10 m/s, Normal load: 150 N/mm).

Numerical Subsurface Damage

Ductile void growth theories can be used to study how a void grows under an imposed stress and strain field. One of the well known relationships used to describe the growth rate of a spherical void in a ductile solid subjected to triaxial stress and strain rate field was developed by Rice and Tracey [14]. They estimated the growth rate of a void of radius R in a ductile and hardening matrix during shear by the following relationship:

$$\dot{R} = \left[\frac{5}{3} + \frac{\sqrt{3}}{2} \frac{\sigma_H}{\sigma_f} \right] \dot{\varepsilon} R \tag{2}$$

where $\dot{R}$ is the void growth rate, σ_H is the mean or hydrostatic stress, σ_f is the equivalent flow stress and $\dot{\varepsilon}$ is the strain rate. Based upon Equation 2 the variation of the damage rate beneath the contact surface can be numerically evaluated with respect to the depth of deformation. To define the void growth rate hydrostatic pressure, flow stress and strain rate distributions determined from the finite element simulations were used.

Figure 9 illustrates the change in normalized void growth rate as a function of normalized depth (z/a) obtained using Equation 2 for a sliding velocity of 10 m/s and normal load of 150 N/mm. Figure 9 shows that the location of the material layer where the maximum rate of damage accumulation occurred was at z/a = 0.06. After the second sliding contact, the maximum value of the normalized void growth rate was calculated as 5×10^{2} s^{-1}. The void growth rate at the close vicinity of the surface z/a < 0.03 was negative, indicating the closing of the voids near the surface due to large hydrostatic pressure. The existing voids at a critical depth (z_C) below the surface corresponding to the maximum value will propagate faster than the voids at other subsurface positions and hence subsurface fracture will occur at this depth.
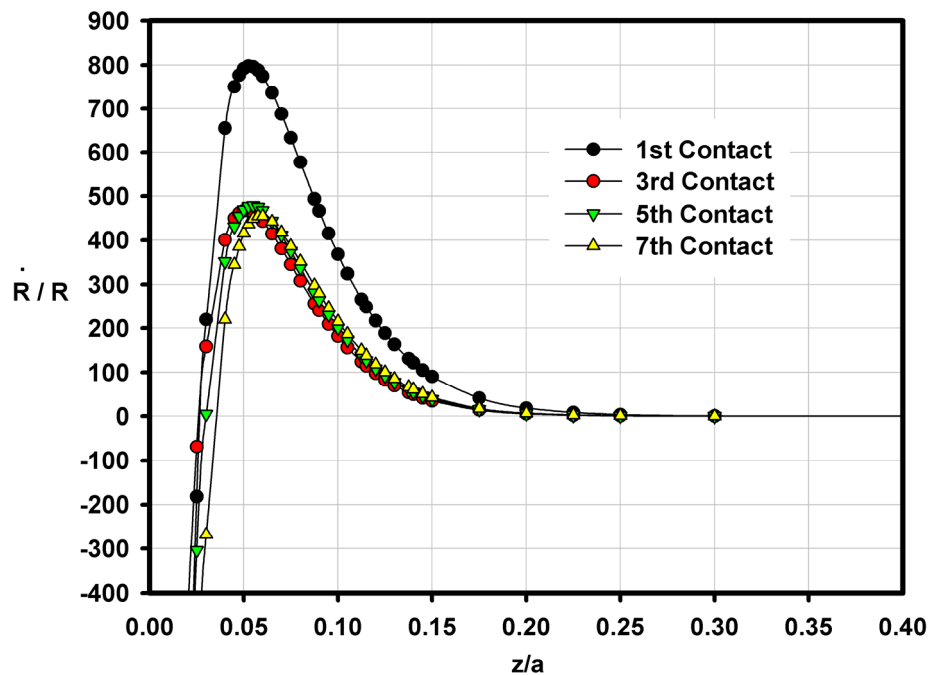

Figure 9: Change in the damage rate with the depth below the contact surface with increasing number of sliding contacts (Sliding velocity: 10 m/s and Normal load: 150 N/mm).

Conclusions

1. Subsurface deformation characteristics of an aluminum alloy during sliding wear were determined using a Lagrangian coupled thermal and mechanical model developed in LS-DYNA. Factors such as strain rate and deformation induced temperature, which plays an important role on the mechanical properties of the sliding surfaces, were considered in the model.

2. Accumulation of subsurface stresses and strains during multiple sliding contacts were investigated. Rapid accumulation of subsurface stresses in the aluminum alloy was reached to a steady state condition after a finite number of the contacts. For a sliding velocity of 10 m/s and a normal load of 150 N/mm, the von Mises stress and the equivalent plastic strain at the contact surface were 514 MPa and 0.19 respectively after the first sliding contact cycle. After the fourth cycle, the stress at the contact surface increased to 586 MPa and the strain to 0.78. Only a 2% increase occurred in the stress between the fourth and seventh (last) cycles while the plastic strain continued to increase to 1.30.

3. Subsurface distributions of the hydrostatic pressure, strain rate and temperature, which is difficult to characterize experimentally or theoretically for work hardening materials, were determined for different loading conditions during sliding contacts. The hydrostatic pressure at the contact surface was 1150 ± 100 MPa between the first and the seventh contacts for a sliding velocity of 10 m/s and a normal load of 150 N/mm. The strain rate ranged from 7.8×10^3 s^{-1} to 9.8×10^3 s^{-1} at a normalized depth of 0.0125. A 45 K temperature increase was observed at the surface after seven sliding contacts.

4. Predicted distributions of stresses and strains were used to model subsurface damage gradient and delamination of subsurface layers. Numerical investigation of a void growth model based on a ductile void growth theory showed the presence of a damage gradient and a critical depth at which delamination cracks might initiate and propagate. For a sliding velocity of 10 m/s and normal load of 150 N/mm, the position of the highest damage rate was calculated to be at a normalized depth of 0.060.

References

1. Suh N.P., "The delamination theory of wear", Wear, vol.25, 1973, pp.111-124.

2. Suh N.P., "Overview of the delamination theory of wear", Wear, vol.44, 1977, pp.1-6.

3. Fleming J.R. and Suh N.P., "Mechanics of crack propagation in delamination wear", Wear, vol.44, 1977, pp.39-56.

4. Jahanmir S. and Suh N.P., "Mechanics of subsurface void nucleation in delamination wear", Wear, vol.44, 1977, pp.17-38.

5. Suh N.P., Saka N., and Jahanmir S., "Implications of the delamination theory on wear minimization", Wear, vol.44, 1977, pp.127-134.

6. Fleming J.R. and Suh N.P., "Relationship between crack propagation rates and wear rates", Wear, vol.44, 1977, pp.57-64.

7. Scott D., "Introduction to tribology", in Fundamental of Tribology, Suh N.P and Saka N. eds., The MIT Press, Cambridge, 1981, pp.1-13.

8. Zhang, J., and Alpas A.T., "Delamination wear in ductile materials containing second phase particles", Materials Science and Eng. A, 1993, vol.A160, pp.25-35.

9. LS-DYNA, Keyword Users Manual, April 2003, Version 970, Livermore Software Technology Corporation.

10. Cowper G.R. and Symonds P.S., Strain hardening and strain rate effects in the impact loading of cantilever beams, Brown University Division of Applied Mathematics Report No. 28, 1957.

11. Johnson G.R., and Cook W.H., "A Constitutive Model and Data for Metals Subjected to Large Strains, High Strain Rates and High Temperatures", presented at the Seventh International Symposium on Ballistics, The Hague, The Netherlands, April 1983, pp.541-547.

12. Jones N., Structural Impact, Cambridge University Press, 1989, pp. 333-352.

13. Metals Handbook, Ninth Edition, vol. 2, Properties and Selection: Nonferrous alloys and pure metals, ASTM, pp.164-167.

14. Rice J.R., and Tracey D.M., "On the ductile enlargement of voids in triaxial stress fields", J. Mech. Phys. Solids, 1969, vol.17, pp.201-217.